TREND

Trapped Radiation Environment Model Development

Time Dependent Radiation-Belt Space Weather Modelling

ESA/TOS-EMA Contract No. 11711/95/NL/JG - CCN 1 to Work Order No. 3

Technical Note 2E

MIR/REM proton maps

M. Kruglanski and P. Bühler
(not complete)

B.I.R.A. – I.A.S.B.	D.E.R.T.S.	P.S.I.
Avenue Circulaire 3 B-1180 Brussel Belgium	ONERA CERT BP 4025 F-31055 Toulouse cedex 4 France	Laboratory for Astrophysics CH-5232 Villigen Switzerland

ESA Technical Management: E.J. Daly (WMA)

MIR/REM Proton maps

This appendix describes the data processing of high-energy proton measurements obtained aboard the Russian Mir space station by the Radiation Environment Monitor (REM) developed by both Compagnie Industrielle Radioélectrique S.A. (CIR) and Paul Scherrer Institute (PSI). The observations cover a period of time from November 1994 to November 1996. The data processing presented here is based on data files provided by PSI in November 1997. The results of this data processing include flux maps for different proton energies, a map of the proton spectrum rigidity and maps of the East-West flux ratio.

The REM detector and the flight parameters are described in the first section. The second section is related to the binning of the MIR/REM measurements. The resulting maps are presented in the third section.

We thank P. Bühler for providing the scientific data files and related documentation.

A.1 Mission and detector description

The REM has been developed by PSI in collaboration with CIR in the frame of the Technology Demonstration Programme of ESA. It has been designed to monitor the radiation environments in a wide range of orbit. A first REM detector was aboard the space technology research vehicle STRV-1B launched in June 94 into a geostationary transfer orbit. A second REM was shipped to the Russian space station Mir in September 1994 as part of the EUROMIR-95 experiment. The principal investigator of REM is A. Zehnder from PSI.

A.1.1 Orbit parameters

The Russian space station Mir is made of different modules, the first of which was launched in February 1986. The Mir station orbits the Earth every 90 minutes on a nearly circular orbit at 52° inclination and 400 km altitude. The altitude os the station perigee and apogee fluctuates in time as a function of the atmospheric drag and the inboard operations. The attitude of the Mir station is approximately 3-axis stabilized, but its orientation can also change according to the inboard operations.

A.1.2 REM description

The technical information on the REM detector presented in this section is mainly collected from two papers of Bühler et al. [A.1][A.2].

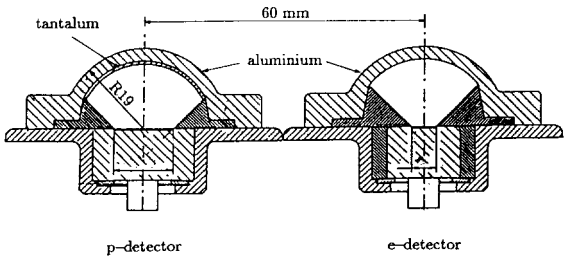

Fig. A.1 Cut view of the two REM sensors. From [A.1].

The REM detector includes of two independent sensors able to measure and accumulate the linear energy transfer (LET) of charged particles passing through. Each sensor consists of a totally depleted silicon surface barrier detectors covered with a spherical dome. The main aperture of both sensors is defined by an aluminium cone with an opening angle of ±45°, mounted on top of the silicon diodes. A cut view of the REM detector is shown in Fig. A.1. The thickness and composition of the spherical domes, and the dimensions of the silicon diodes have been optimized for particle discrimination and processable count rates. The main characteristics are summarized in Table A.1. Both sensors have an aluminium shielding. The p-detector has an additional shielding of tantalum to reduce the penetration of electrons in the energy range 1–10 MeV and to better monitor the proton radiation environment The backside of both sensors is shielded by the detector housing and the spacecraft, i.e. the Mir station.

Table A.1 Main characteristic of the REM detector aboard the Mir station. From [A.1].

Sensor	Sensitive area of silicon diode (mm^2)	Thickness of silicon diode (µm)	Dome thickness and material	Electron threshold energy (MeV)	Proton threshold energy (MeV)
p-detector	150	330	3 mm Al 0.75 mm Ta	2.6	34.0
e-detector	25	267	0.71 mm Al	0.7	10.0

The charge pulses produced by particle passing through a silicon diode are measured by a charge sensitive pre-amplifier linked to a 12-bit analog-to-digital convertisor (ADC). A programmable compression function reduces the ADC outputs into a 16-bin histograms. Each histogram bin, i.e. channel, corresponds to a given range of deposited energy. The mean energies deposit ΔE_i per count for each channel *i* are listed in Table A.2. Note that the three first channel of each sensor are contaminated with noise and can not be used.

A built-in pulser connected at the input of the pre-amplifiers allows to check in-flight for proper functioning of the electronics and for dead-time determination. Data is successively accumulated during 31.9 seconds.

The response of the REM detector to incident particle fluxes is expressed by a geometric factor $G_k(E, i)$ per channel *i* for each particle species *k* (p, e, ions) of energy *E* average over all incident

Table A.2 Mean energies deposit per count in the REM sensors (in keV).

Channel	p-detector	e-detector
01	<1.0	<13.0
02	16.5	28.5
03	93.0	105.0
04	185.0	196.5
05	246.5	257.5
06	307.5	319.0
07	384.0	395.5
08	491.0	502.5
09	613.5	625.0
10	782.0	793.0
11	1074.5	1085.0
12	1825.0	1835.0
13	5390.0	5390.0
14	15295.0	15290.0
15	72100.0	72100.0
16	>100,000.0	>100,000.0

angles. The geometric factors were determined by Monte Carlo simulations and calibration experiments with 45–300 MeV protons and 1–10 MeV electrons. The energy response of the REM detector is determined by the dome shielding (lower energy cutoffs) and by the energy dependence of the LET function. Note that the large opening angle of the sensors limits the energy resolution.

One should note that the count rates met by the REM detector aboard the Mir station are sufficiently weak, so that the dead-time correction can be neglected. But, too weak to allow the transformation of a single measurements into proton or electron fluxes. A such transformation can only be performed on multiple measurements.

A.2 Data processing

The MIR/REM data files provided PSI have been processed to build flux maps of the inner edge ($L < 2$) of the trapped proton population. In order to make the data portable across various computer platforms, the Common Data Format (CDF) developed by the National Space Science Data Center (NSSDC) is used to store intermediate and final results. The CDF software is available via internet on `http://nssdc.gsfc.nasa.gov/cdf/cdf_home.html`.

A.2.1 Data retrieval

The PSI data files consist of a set of 1254 CDF files for the period of time from November 1994 to November 1996. There exist two files per calendar day named “MAyymmdd.CDF” and

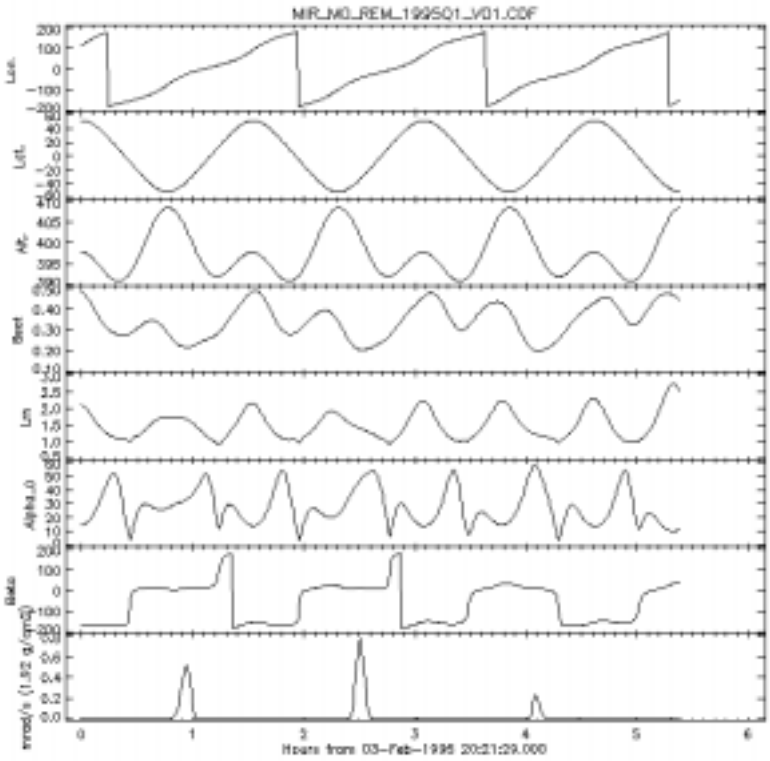

Fig. A.2 Sample of ephemeris and dose data recorded by the MIR/REM experiment.

“MByymmdd.CDF”, respectively, where the six characters “yymmdd” refer to the day of observation (year, month, day). The “MAyymmdd.CDF” files contain the central time of the measurements, the accumulation time, the count rate for each channel and the house keeping data (temperatures, voltages, test pulser data). The “MByymmdd.CDF” files contain the GEI cartesian coordinates of the Mir station, the pointing direction of the REM detector, and the (B,L) values at the Mir location computed with the magnetic field models IGRF 95 [A.3] and Tsyganenko 1989 [A.4] (Kp = 0).

The ephemeris and count rate data have been retrieved and processed per block of three months. For each data point,

- the Mir location has been converted into geodetic altitude, latitude and longitude;
- the detector orientation with respect of the local magnetic field has been deduced;
- the magnetic field intensity and the *L* parameter have been re-evaluated;
- the count rates have been filtered for suspicious data and transformed into counts;
- restrict dose rates have been calculated for each sensor.

The results have been stored in CDF files named “MIR_M0_REM_yyyyQq_Vvv.CDF” where the characters “yyyy”, “q” and “vv” refer to year, quarter and version number, respectively. The different transformations have been make with the help of the version 1.13 of the UNILIB software library [A.5]. The UNILIB software is available via internet on `http://www.magnet.oma.be/home/unilib/home.htm`.

After geometric transformations, the look direction of the REM detector is characterized by a pair of polar and azimuthal angles (α, β) measured [A.6] in a coordinate system attached to the local magnetic field line passing through the current Mir location. The coordinate system is such

that the *z*-axis points in the direction of the magnetic field vector, and the *x*-axis points in the direction of the normal to the magnetic field line. The angle β is associated to the East-West asymmetry, and the angle α to the pitch angle of the detected particles. Note that our evaluation of the McIlwain's parameter *L* [A.7] takes into account the value of α.

The restricted dose rates are calculated with the help of Table A.2 by the relation

$$D = \sum_i c_i \Delta E_i \qquad \text{(A.1)}$$

where c_i is the count rates in channel *i*, and the sum runs over the higher 13 channels of the sensor since the three first channels of both REM sensors are contaminated by noise.

As a sample of the MIR/REM data is shown in Fig. A.2. The figure includes the geodetic longitude, latitude and altitude of the Mir station, the magnetic field intensity at this location, the parameters *L* and α_0, the azimuthal angle β and the restricted dose rate beyond 0,71 mm of aluminium. Three successive crosses of the South Atlantic Anomaly region occurs during the 5 hours covered by Fig. A.2. In both cases, *L* is less than 2 and the magnetic field intensity is near a minimum and β is about zero. The higher peak corresponds to a dose rate about 0.8 mrad/s.

A.2.2 Data binning

The MIR/REM have been binned on a mesh in $(\alpha, \beta, L, \alpha_0)$. The number of bins for each dimension and the bin limits are given in Table A.3. The binning in (α, β) is quite rough. In the data reduction phase, only the bins for which

$$80 < \alpha \leq 90 \text{ and } -120 < \beta \leq -60 \qquad \text{(A.2)}$$

$$\text{or } \; 80 < \alpha \leq 90 \text{ and } 60 < \beta \leq 120 \qquad \text{(A.3)}$$

will be taken into account. The two cases correspond to measurements associated to locally mirroring particles coming from the West or from the East, respectively. The other bins in (α, β) are only present for checking purposes. The binning in *L* is limited to values less than 2. In α_0, all the angles are covered by the binning. Note that the binning has not been applied to the three first channels of both sensors since it has been proved that they are contaminated. The binning results have been stored in CDF files named "MIR_M1_REM_yyyyQq_Vvv.CDF" with the same naming convention. They include for each bin and for each channel

- the number of data points,
- the sum of the counts,
- the sum of the counts to the square.

To improve the statistic, one year files (named "MIR_M2_REM_yyyy_Vvv.CDF") have been created by summation of the contents of four consecutive files.

The distribution of the MIR/REM measurements on the $(\alpha, \beta, L, \alpha_0)$ mesh is illustrated on Figs. A.3 and A.4 for the year 1995. In both figures, only the measurements corresponding to locally mirroring particles $(80 < \alpha \leq 90)$ are take into account. In the left hand panel of Fig. A.3, the number of measurements is shown as a function of β and *L*. The last bin in *L* is not represented. For small *L* values, the most populated bins are the bins which satisfy Eqs. (A.2) or (A.3). For larger value of *L*, the distribution in azimuthal angle is more homogene. The distribution of the measurements as a function of β and α_0 is shown on the right hand panel of Fig. A.3. There is a poor coverage in the equatorial region ($\alpha_0 \sim 90$) due to the low altitude of the Mir orbit. More-

Table A.3 Bin limits used for the MIR/REM data binning

Variable	Number of bins	Bin limits
α	3	0, 60, 80, 90
β	6	-180, -120, -60, 0, 60, 120, 180
L	22	0.975, 1.025, 1.075,..., 1.975, 2.025, 5
α_0	18	0, 7.5, 12.5, 17.5,..., 87.5, 90

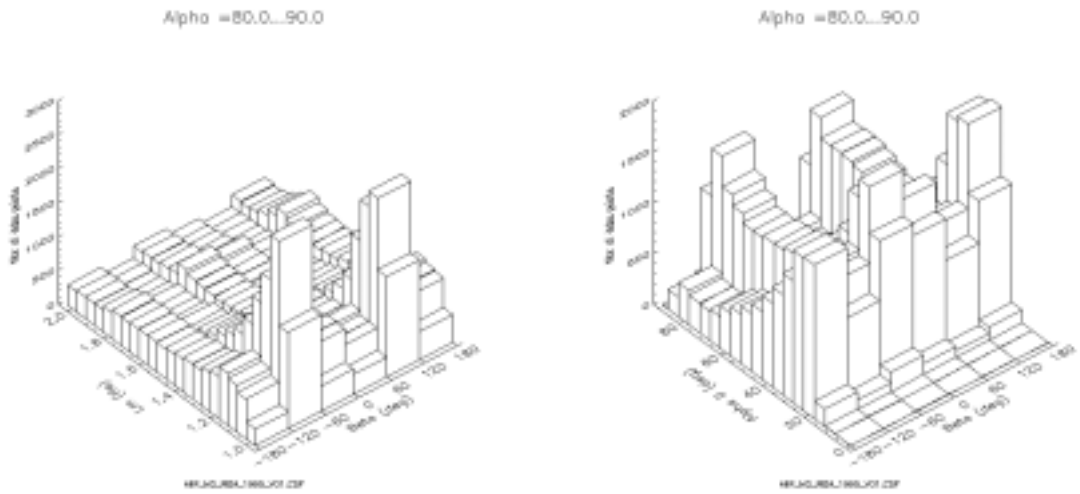

Fig. A.3 Distribution of the MIR/REM measurements in the (β, L) and (β, α_0) spaces.

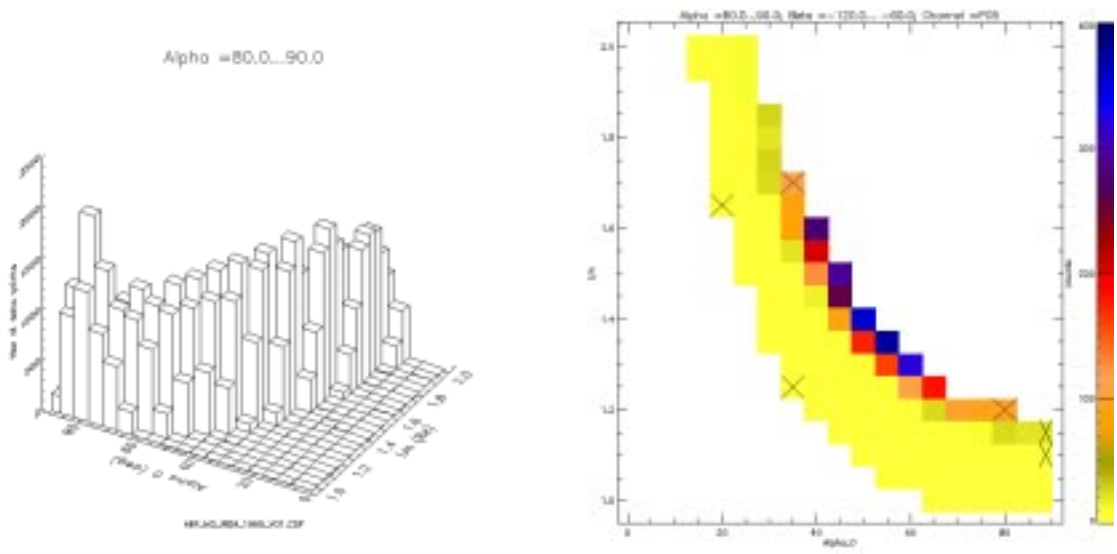

Fig. A.4 Distribution of the MIR/REM measurements in the (L, α_0) space and sample of count measurements average over one year data.

over, the bins which satisfy Eqs. (A.2) or (A.3) are more populated for small values of the equatorial pitch angle, i.e. near or inside the loss cone.

The left panel of Fig. A.4 shows the distribution of the MIR/REM measurements as a function of L and α_0. The different bins are clearly not equally populated by the measurements. This particular distribution is due to the Mir orbit and to the restriction on the local pitch angle. Since the particles which are mirroring above the Mir altitude can not be observed, particles with a large equatorial pitch angle can only be observed at very low L values ($L < 1.2$). At larger L, only particles with a small equatorial pitch angle, i.e. near the loss cone, can be observed. On the other hand, since only the locally mirroring particle are take into account, particles with a small equatorial pitch angle are not observed in the low L region. To better illustrate the distribution of the MIR/REM measurements, the average of the counts for the channel P05 when $-120 < \beta \leq -60$ is shown on the right panel of Fig. A.4 as a function of L and α_0. The channel P05 contains detections of protons with incident energies above 200 MeV. It appears clearly from the figure that only the most inner edge of the proton radiation belt is covered by the MIR/REM measurements. The crosses indicates the bin of which there is less than 15 measurements during 1995. Proton flux measurements are mainly located for α_0 values between 30 and 70 degrees and L values between 1.2 and 1.7. Outside this range, there is no measurements or the proton flux is negligible. Nevertheless, the MIR/REM measurements are useful to study the long-time fluctuation of the loss cone, the East-West asymmetry, and, the radiation environment at altitudes of MIR [A.8].

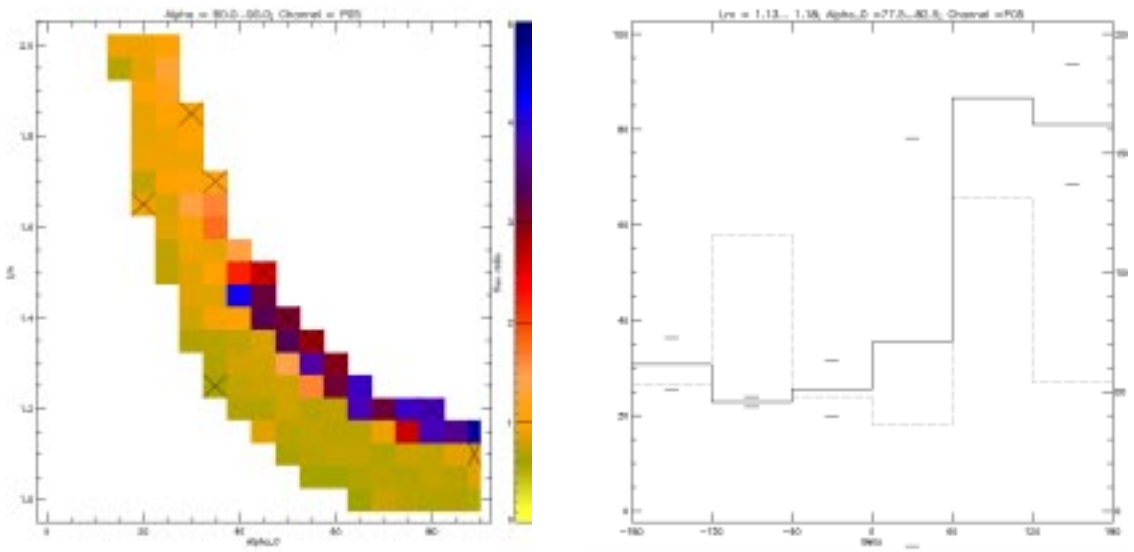

Fig. A.5 MIR/REM Observation of the East-West asymmetry

The potentiality of the MIR/REM database to study the East-West asymmetry is illustrated on Fig. A.5. On the left hand panel of this figure, the East/West ratio of the counts in the channel P05 is presented as a function of L and α_0. The East and West directions are defined by Eqs. A.2 and A.3, respectively. According to the theory [A.6], the East/West ratio is significant when large variations of the counts with L are observed, e.g. at the most inner edge of the radiation belt. In Fig. A.5, the East/West ratio is about 1, except in a small region were it increase by a factor about 5. This region corresponds in Fig. A.4 where a gradient of the counts is present. The right hand panel of Fig. A.5 shows the variation of the counts with β for the bin where $L \sim 1.15$ and $\alpha_0 \sim 80$. The solid and dotted lines correspond to the average counts and the number of measurements, respectively. The small ticks correspond to the mean value plus/minus one standard deviation. For this particular bin, the East/West ratio is about 4. Note that most of the measurements correspond to values of the azimuthal angle near ±90.

A.2.3 Field of view correction

Due to its field of view (±45°), the MIR/REM detector measures neither omnidirectional nor directional fluxes. Since the proton flux is highly anisotropic at low altitudes, a simple rule of three can not be used to transform observed flux into directional or omnidirectional data: the data have to be deconvoluated. Nevertheless an angular deconvolution such as the one applied by Heynderickx and Kruglanski [A.9] for EI88/AZUR, PET/SAMPEX and HEPS/UARS measurements can not be used in the case of the MIR/REM measurements without several doubtful assumptions. In order to determine directional data from the MIR/REM measurements without a large set of assumptions, we limit our analysis to the measurements for which omnidirectional data can be easily deduced. The method of Badhwar and Konradi [A.10] is then applied to transform omnidirectional data into directional fluxes.

At low altitudes, almost all the observed protons are near their mirror points, i.e. in direction with a local pitch angle near to 90°. Therefore, it can be reasonably assumed that the measurements for which $80 < \alpha \leq 90$ corresponds to omnidirectional data with respect to the pitch angle. This assumption will not be satisfied when the local value of the loss cone becomes larger than 30°. In order to take into account the East-West asymmetry of the proton fluxes, the data have to be averaged over all the azimuthal direction. so, taking into account the field of view of the detector, the MIR/REM measurements can be transform to omnidirectional counts by

$$C^{\text{omni}}_{\alpha_0, L} = \frac{360}{90} \times \langle C^{80 < \alpha \leq 90}_{\alpha_0, L} \rangle_{\beta} \qquad \text{(A.4)}$$

where the counts at $80 < \alpha \leq 90$ are averaged over the bins in β. When the counts are reduced into omnidirectional fluxes, the method of Badhwar and Konradi [A.10] can then be applied to obtain directional fluxes. To this effect, the binned data has been to a mesh in (L, α_0) which includes per channel for each bin:

- the mean omnidirectional count $C^{\text{omni}}_{\alpha_0, L}$,
- the East-West count ratio, and,
- the standard deviations of both values.

The 3-month binning results are stored in the CDF files “MIR_M3_REM_yyyyQq_Vvv.CDF” with the same naming convention as the previous files

A.2.4 Data reduction (to be done!)

The count rates c_i^{omni} measured by the MIR/REM detector are related to the omnidirectional proton and electron fluxes (f_p, f_e) and the geometric factors by [A.1]

$$c_i^{\text{omni}} = \int f_p(E) G_p(E, i) dE + \int f_e(E) G_e(E, i) dE . \qquad \text{(A.5)}$$

When the particle energy spectra are approximated by step functions, Eq. (A.5) is reduced to the resolution of a linear problem which is solved by a least square algorithm. For the MIR/REM data, the proton and electrum spectra are defined with the help of 5 and 3 energy bins, respectively. The energy ranges are given in Table A.4. The algorithm has been applied by PSI to convert the mean omnidirectional counts and East-West count ratios into omnidirectional differential proton fluxes and East-West flux ratios for the five energy range of Table A.4.

To be continued...

Table A.4 Ranges of the energy bins used to describe the proton and electron spectra

bin	f_p	f_e
1	– MeV	– MeV
2	– MeV	– MeV
3	– MeV	– MeV
4	– MeV	
5	– MeV	

Note for Paul

Let C and R be the mean count and the East-West count ratio. The “East” and “West” counts are given by

$$\begin{bmatrix} C_E \\ C_W \end{bmatrix} = \frac{2}{1+R} \begin{bmatrix} R \\ 1 \end{bmatrix} C \tag{A.6}$$

and the relative errors by

$$\begin{bmatrix} \Delta C_E / C_E \\ \Delta C_W / C_W \end{bmatrix} = \frac{\Delta R}{1+R} \begin{bmatrix} R^{-1} \\ 1 \end{bmatrix} + \frac{\Delta C}{C} \tag{A.7}$$

So it is possible to apply your algorithm to deduce omnidirectional differential fluxes, East-West flux ratio, and to estimate an error for both values. The error is given by the sum of the least square value with the sum of the standard deviations propagated trough the linear system

A.3 Final flux maps

References

[A.1] Bühler, P., S. Ljungfelt, A. Mchedlishvili, N. Schlumpf, A. Zehnder, L. Adams, E. Daly, and R. Nickson, Radiation environment monitor, *Nucl. Instr. Meth. Phys. Res., A 386*, 825–831, 1996

[A.2] Bühler, P., L. Desorgher, A. Zehnder, E. Daly, and L. Adams, Observations of the low earth orbit radiation environment from Mir, *Radiat. Meas., 26*, 971–921, 1996

[A.3] Barton, C.E., International geomagnetic reference field: The seventh generation, *J. geomag. geoelec.*, 49, 123–148, 1997

[A.4] Tsyganenko, N.A., A magnetospheric magnetic field model with a wrapped tail current sheet, *Planet.Space.Sci.*, 37, 5–20, 1989

[A.5] Heynderickx, D., and M. Kruglanski, Unirad improvements and subroutine library, Technical Note 10, ESA contract N° 10725/94/NL/JG(SG), April 1998

[A.6] Kruglanski, M., and D. Heynderickx, Improvement of the trapped proton anisotropy description, Technical Note 6 part 2, ESA contract N° 10725/94/NL/JG(SG), April 1998

[A.7] McIlwain, C.E., Coordinates for mapping the distribution of magnetically trapped particles, *J. Geophys. Res.*, 66, 3681–3691, 1961

[A.8] Bühler, P., L. Desorgher, A. Zehnder, E. Daly, and L. Adams, REM Measurements aboard Mir during 1995, PSI-PR-97-02, Paul Scherrer Institute, January 1997

[A.9] Heynderickx, D., and M. Kruglanski, Flight data comparisons, Technical Note 5, ESA contract N° 10725/94/NL/JG(SG), June 1998

[A.10] Badhwar, G.D., and A. Konradi, Conversion of omnidirectional proton fluxes into a pitch angle distribution, J. Spacecraft and Roc., 27, 350–???, 1990

To appear in the *SREW Proceedings*, 2000.

Energy and spatial dependence of the east-west effect observed by Mir-REM

Paul Bühler, Alex Zehnder,

Paul Scherrer Institute, Laboratory for Astrophysics, 5232 Villigen, PSI, Switzerland

Michel Kruglanski

Belgian Institute for Space Aeronomy, 1180 Brussels, Belgium

Eamonn Daly

ESTEC, NL-2200 AG Noordwijk, The Netherlands

Abstract

In the South Atlantic Anomaly the energetic proton fluxes are anisotropic. Fluxes from west are higher than those from east. Using data from the Radiation Environment Monitor aboard the Russian orbital station Mir, we determined the energy and spatial dependence of the west-east proton flux ratio. We find the energy spectra of the east-fluxes to be softer than those from west, and the effect to be a decreasing function of the L-shell parameter, which vanishes above $L \approx 1.7\, R_E$. Comparison with model calculations show that existing models used to describe the anisotropy can not reproduce the observed characteristics.

1. Introduction

The LEO orbits are the preferred orbits for manned space missions, like Mir, Space Shuttle, ISS. In such an orbit an important contribution to the total radiation dose occurs in the South Atlantic Anomaly, SAA [*Konradi et al.,* 1994; *Badhwar et al.,* 1996; *Bühler et al.,* 1996] and is caused by the high energetic trapped protons of the inner radiation belt. It is therefore of vital interest to have accurate models of this particle population.

A special feature of the SAA is the anisotropy of the proton fluxes. The anisotropy is caused by the fact, that at a given position trapped particles arriving from different directions have their guiding centers at different locations and therefore belong to different drift-shells. This is true anywhere in the magnetosphere. But if the difference in guiding center position is large compared to the scale length of the spatial flux gradient then the locally observed flux distribution can be expected to be anisotropic [*Lenchek and Singer,* 1962].

At low altitudes the trapped proton population is controlled by the Earth's atmospheric density and its altitude gradient, which leads to strong flux gradients in the SAA. The difference in guiding center location for particles arriving from opposite directions scales with the gyro-radius. The gyro-radius depends on the particle's momentum p, and on the magnetic field strength, B with $r_{gyro} = p/(q \cdot B)$. The anisotropy is therefore best observed with high momentum particles at low magnetic fields. The Russian orbital station Mir encounters the minimum field strength of approximately 0.2 *Gauss* in the SAA. There the gyro-radius of 100 MeV protons is of the order of 100 km and comparable in size with the scale length of the flux gradients. It is therefore the proton fluxes in the SAA for which the anisotropy can be best observed.

The effect is a function of energy and can also be expected to depend on the local magnetic field configuration, thus to be a function of magnetic coordinates B and L-shell parameter, L. The effect has been measured at selected locations and energies [*Heckman and Nakano,* 1969; *Konradi et al.,* 1994; *Looper et al.,* 1998; *Bühler et al.,* 1998] and has been shown to be important.

In this paper we investigate the spatial and energy dependence of the difference in proton fluxes arriving from magnetic east and west, in the SAA.

2. Observations and data analysis

2.1. Observations

For this analysis we used proton data from the Radiation Environment Monitor, REM aboard Mir [*Bühler et al.,* 1996]. REM was mounted outside the Mir space station and was working from November 1994 to November 1996. REM consists of two independent shielded silicon detectors and measures the energy deposit of charged particles. Data was accumulated and binned into 32 energy deposit bins with a temporal resolution of 32 seconds. The shieldings of the detectors consist of a thick aluminium cone and spherical shields of aluminium and tantalum of $> 0.19\ g/cm^2$ for one of the detectors and and $> 2.06\ g/cm^2$ for the other detector. The lower proton energy threshold is therefore around 10 MeV. Whereas the heavier shield of one detector efficiently stops electrons of several MeV, the lower energy threshold for electrons of the less shielded detector is around 1 MeV.

The aluminium cone restricts the direct field of view of the detectors to $\pm 45°$. REM was mounted at the outside of Mir and was therefore very well shielded from the backside by the space station.

Mir is in a practically circular Low Earth Orbit, LEO, at an altitude of $\approx 400\ km$, an inclination of 52°, and a period of 90 minutes. It scans several times per day through the SAA region, with varying orientation.

2.2. Data mapping

For each Mir-REM data point we determined the satellite position $\vec{s}$ and the look direction of REM, $\vec{o}_{REM}$, for which the necessary information was provided by the Mir control center ENERGIA, and computed the local magnetic field vector, $\vec{B}$, and L-shell parameter, L for locally mirroring particles with the IGRF 95 magnetic field model.

We then selected data points in the inner radiation belt ($1.1 < L < 2.6$) for which the cosine of the angle between $\vec{o}_{REM}$ and magnetic east or west was larger than 0.81, where magnetic east and west are defined by $-\vec{s} \wedge \vec{B}$ and $\vec{s} \wedge \vec{B}$, respectively. The two groups of data, east and west, were then binned into B-L-bins of 0.05 R_E and 0.001 *Gauss*. The histograms in each bin were finally averaged over the entire mission. In such a way we obtained temporally averaged B-L-maps of REM histograms for east and west looking REM orientations.

Figure 1 shows an extract of the such determined

Figure 1

maps at $1.3 < L < 1.35\ R_E$. In the large panel the count rates of the heavier shielded detector (sum of detector channels 4 and 5, representing $> 200\ MeV$ protons) is plotted versus B. The asterisks show the data with REM looking in magnetic west direction, and the diamonds the data with REM looking in magnetic east direction. The dashed lines show the background corrected count rates. Over a large range of B-values, which covers a flux range of more than two orders of magnitude, the west-rates are significantly higher than the east-rates . At large B-values the two curves merge and flatten out. There the proton fluxes are very low and the REM count rates are dominated by electrons and cosmics. This part is used to determine the background.

The two small panels show the relative count rate histograms of the heavier shielded detector in a selected B-bin ($0.199 < B < 0.200\ Gauss$) for REM looking west (upper panel) and REM looking east (lower panel). The shapes of the histograms allow to qualitatively judge the energy spectrum of the incident particles. Compared with the west-histograms, the east-histograms are biased towards the higher channels, indicating the east spectra to be softer than the west spectra. This indeed can be expected since the high energy particles coming from east are members of drift shells dipping on average deepest into the atmosphere which explains why the east fluxes are low and their spectra soft.

2.3. Spectral information

The REM histograms can be used to deduce the incident particle energy spectra. The count rate in detector channel i, cr_i in units of $1/sec$ is related to the incident differential particle spectra $f_k(E)$, where index k indicates the particle species, by

$$cr_i = \sum_k \int_0^\infty f_k(E) \cdot G_k(i,E) dE \qquad (1)$$

$f_k(E)$ is given in units of $1/sec/cm^2/MeV$ and $G_k(i,E)$ is the energy, detector channel, and particle species dependent geometric factor and is given in units of cm^2. The geometric factors were determined by calibrations in a proton beam and betatron, and with numerical simulations including a model for the mass distribution of the space station [*Ljungfelt,* 1993; *Hajdas et al.,* 1993]. For the analysis of the REM data in the SAA we assume only protons and electrons to be relevant and neglect any other contribution to the detections.

In order to invert equation (1) the proton and electron spectra are parameterized. We approximated the shape of the proton energy spectra by a power law, $f_p(E) = f_p(E_{p0}) \cdot (E/E_{p0})^{\gamma_p}$ with $E_{p0} = 30\ MeV$ and the shape of the electron spectra by an exponential function, $f_e(E) = f_e(E_{e0}) \cdot exp(-\gamma_e \cdot (E - E_{e0}))$ with $E_{e0} = 1.0\ MeV$. The normalizations and spectral indices are free parameters and are simultaneously determined by a numerical fit of the measured detector count rates with equation (1). The method yields good proton spectral characterization only in B-L-bins where the proton fluxes contribute a non-neglectable number of counts to the count rates. This is the case at $1.1 < L < 2.2\ R_E$ and the low B-values.

The left panel of figure 2 shows a grey-scale B-L-map of the $100\ MeV$ proton flux west-east ratio. Note, that the white area below the grey shaded area is not sampled by Mir, and that in the white area above, the proton contribution is too small to allow the determination of proton spectral parameters with REM. The right panel shows analogously the west-east ratio of the proton spectral indices.

figure 2

The east-west effect is clearly a function of L. The flux ratio is largest at small L, continuously decreases with increasing L, and becomes 1 above $L \approx 1.7\ R_E$. The same behavior is also found for the spectral index. Below $L \approx 1.7\ R_E$ the east spectra are softer than the west spectra, as indicated by the histograms shown in figure 1, but the difference decreases with increasing L. For a given L-bin there is no obvious magnetic field dependence.

3. Comparison with models

In the following we compare the REM measurements with two models of the east-west effect and especially address the question whether the models are able to describe the observed L-dependence.

3.1. Local model

Lenchek and Singer, 1962 argued that the flux gradients in the SAA are mainly caused by the interaction of the particles with the upper atmosphere and that the proton fluxes in first approximation could be directly related to the gyration averaged atmospheric density. But since the atmospheric density is a function of altitude, the proton fluxes could be expressed as function of altitude of their guiding centers.

The difference in altitude of the guiding center and

the point of observation, dh is given by

$$dh = r_{gyro}(E)cos(I)sin(\beta) \quad (2)$$

where I is the dip angle of the local magnetic field line, and β is the azimuthal angle, with $\beta = -90°$ is east and $\beta = +90°$ is west.

In the following it is assumed, as done by *Lenchek and Singer* [1962], that the proton fluxes are inversely proportional to the atmospheric density, ρ_{atm} at the guiding center location. Then using different approaches for the altitude dependence of the atmospheric density and equation (2), the west-east flux ratio can be calculated. In table 1 two cases are listed. Both models have a free parameter, which can be computed by applying the formulas in the last column of table 1 to the data.

We have done that for the B-L-bins with the lowest B-values at a given L. The results are presented in figure 3 as function of L. The two uppermost panels contain the proton flux normalization at 30 MeV and the spectral power law indices, respectively. The lines without dots are smoothed curves through the data points. The following panels show the cosine of the averaged magnetic field dip angle in the given B-L-bin, the proton flux ratio, H_0, and n at 50 (bold line), 100 (dotted line), and 200 MeV (dashed line), respectively. The curves without dots in the three lowermost panels show the results computed with the smoothed curves of the two uppermost panels.

The resulting atmospheric scale height H_0 increases continuously from around 100 km at $L = 1.1\ R_E$ to about 300 km at $L = 1.6\ R_E$ but then starts to attain unreasonable values. This is a consequence of the formula for H_0 given in table 1. When the flux ratio f_{west}/f_{east} approaches the value 1, the denominator becomes very small, and thus H_0 grows infinitively. At lower L-values the H_0 value compares not too badly with the ≈ 60 km found by *Heckman and Nakano* [1963]. However, since H_0 is thought to be a characteristic quantity of the atmosphere there is no obvious reason why it should depend on L. The same is true for the altitude power law index n. However, n has no singularity and is a smooth function of L. *Heckman and Nakano* [1969] found n to be around 4 to 5, which is somewhat higher than our results. We must remind here that REM has a rather large acceptance angle such that therefore the 'true' east-west ratio can be expected to be higher than the values we measure with REM. So the 'true' H_0 can be expected to be smaller and the 'true' n, larger than our results.

If we assume H_0 and n to be independent of L, the L-dependence of the east-west effect must be given by the L-dependence of dh, which, according to equation (2) is defined by the L-dependence of the magnetic dip angle I. In this case the east-west ratio can reach the value 1 only where $I = 90°$, which however is nowhere the case (see panel 4 of figure 3) in the investigated region.

Although the Lenchek-Singer model of the east-west effect may give reasonable results in selected areas, it can not describe the observed L-dependence of the east-west effect in a consistent way.

3.2. Generalized model

Kruglanski et al. [1998] assumed that the directional proton flux at a given location, $f(E, \alpha, \beta)$ is the perpendicular flux at the guiding center location and can be written as

$$f(E, \alpha, \beta) = f_\perp(E, B_{GC}, L_{GC}) \quad (3)$$

where B_{GC} and L_{GC} are the magnetic field strength and L-value at the guiding center location of the particles. α is the pitch angle and β the azimuthal angle. In order to avoid the calculation of B_{GC} and L_{GC} they expanded the expression in equation (3) to first order in L and in addition made the approximation $B_{GC} = B$. The derived expression for the directional proton flux is

$$f(E, \alpha, \beta) \approx f_\perp(E, B, L) + \Delta L \cdot \left.\frac{\partial f_\perp}{\partial L}\right|_{E,B} \quad (4)$$

where $\Delta L = L_{GC} - L$. They further derived an analytical expression for ΔL which only depends on local quantities such that the directional proton flux can be expressed as

$$f(E, \alpha, \beta) \approx f_\perp(E, B, L) + \left(\frac{E^2 + 2m_0c^2E}{qc\sqrt{MBL^{-3}}}\right) sin\beta \cdot \left.\frac{\partial f_\perp}{\partial L}\right|_{E,B} \quad (5)$$

with m_0 the proton rest mass, q the proton charge, and M the earth's magnetic dipole moment.

With this approximation the west-east flux ratio for locally mirroring particles can be expressed as

$$f_{west}/f_{east} = \frac{f(E, 90°, 90°)}{f(E, 90°, -90°)} \quad (6)$$

Besides some fundamental constants this relation contains only local quantities, the perpendicular flux $f_\perp(E, B, L)$ and its derivative $\left.\frac{\partial f_\perp}{\partial L}\right|_{E,B}$.

Equation (6) can be solved for $\frac{\partial f_\perp}{\partial L}$ and using the measured west-east flux ratios and $f_\perp(E,B,L) = (f_{west} + f_{east})/2$, $\frac{\partial f_\perp}{\partial L}$ is determined. The result of this computation is shown in figure 4. Like in figure 3, we show the results for the B-L-bins with the lowest B value at a given L and plot them as function of L. The panels show (t.t.b) our estimate of $f_\perp$, the derivation of $f_\perp$, and the derived $\frac{\partial f_\perp}{\partial L}$ at 50 (bold line), 100 (dotted line), and 200 MeV (dashed line), respectively. The smooth curves without dots are computed with the smoothed spectral normalization and power law index curves shown in the two uppermost panels of figure 3.

Although the derivative of $f_\perp$ shown in the middle panel is not taken at B = const we can use it for qualitative comparisons with the derived $\frac{\partial f_\perp}{\partial L}$ (this is justified by $\left.\frac{\partial f_p}{\partial L}\right|_{B,E}$ versus L curves calculated with AP8 model fluxes, which show a similar L-dependence as the curves shown in the middle panel of figure 4). There are significant differences between the two sets of curves. According to equations (5) and (6) the west-east ratio becomes 1 where $\left.\frac{\partial f_p}{\partial L}\right|_{B,E} = 0$ or where $f_\perp$ as function of L has a local maximum. The positions of the maxima of $f_\perp$ depend slightly on energy but are around 1.4 to 1.5 R_E which is definitively lower than the position where the measured west-east ratio becomes 1.

The Kruglanski model takes the flux gradients along L into account but neglects the gradients along B. This approximation is only valid as long as $dB = B_{GC,west} - B_{GC,east}$ is smaller than the scale length of the flux gradients along B. Assuming, that the east and west guiding centers are separated by a gyrodiameter we find that for 200 MeV protons dB is a function of L and decreases from around 0.02 $Gauss$ at L = 1.1 R_E to approximately 0.005 $Gauss$ at L = 2 R_E. Figure 1 shows that these dB-values are important compared to the scale length of the flux gradients along B. The neglection of a dB term in equation (4) may therefore not be justified in the relevant B-L-area. These estimates show further that dB is a decreasing function of L and therefore shows the same trend as the west-east ratio. dL in contrary increases with L, from around 0.2 R_E at $L = 1.1$ R_E to below 0.1 R_E at L = 2 R_E This might indicate, that the dB-term may even be dominating. It is interesting to note, that dB and dL in a given L-bin are practically independent of B and therefore the east-west effect, in first approximation can be expected not to depend on B, which is in agreement with our measurements (see figure 2).

4. Summary and conclusions

When comparing the presented measurements with model calculations and other observations it must be kept in mind that the presented measurements have been made with a wide-angle instrument. As a consequence the measured west-east ratios represent a lower limit for the true values. This affects the absolute values but not the qualitative characteristics, like the energy and L-dependence.

The measurements show, that

- over a wide L and B range the proton fluxes arriving from west are higher than the particle fluxes coming from east
- the east-spectra are softer than the west-spectra
- the west-east ratio is a decreasing function of L and becomes 1 above $L \approx 1.7$ R_E

Non of the three models tested here can describe the observed L-dependence in a consistent way. They all use approximations which, although giving good results at selected locations, may not be valid over a larger area. The presented results may be used as a guideline for the development of improved models.

Acknowledgments. This work was supported by ESA's Technology Research Program, ESA/TOS-EMA, Space Environments and Effects Major Axis.

References

Badhwar, G.D., Atwell, W., Cash, B., Petrov, V.M., Akatov, Y.A., Tchernyk, I.V., Shurshakov, V.A., and Arkhangelsky, V.A., Radiation environment on the Mir orbital station during solar minimum, *Adv. Space Res., ??*, ??, 199?.

Bühler, P., Desorgher, L., Zehnder, A., Daly, E., Adams, L., Observations of the low earth orbit radiation environmnet from Mir, *Rad. Measurements, 26,* 917, 1996.

Bühler, P., Ljungfelt, S., Mchedlishvili, A., Schlumpf, N., Zehnder, A., Adams, L., Daly, E., Nickson, R., Radiation environment monitor, *Nucl. Instr. and Meth. in Phys. Res. A, 368*, 825, 1996.

Bühler, P., Desorgher, L., Zehnder, A., Daly, E., Adams, L., REM measurements aboard Mir during 1995, *Adv. Space Res., 21,* 1645, 1998.

Hajdas, W., Ljungfelt, S., and Cordt, I., Test of the REM detector on the betatron, *Ann. Report, IIIA,*, 155 pp.,

Paul Scherrer Institute, 5232 Villigen PSI, Switzerland, 1993

Heckman, H.H. and Nakano, G.H., East-west asymmetry in the flux of mirroring geomagnetically trapped protons, *J. Geophys. Res., 68,* 2117, 1963

Heckman, H.H. and Nakano, G.H., Low-altitude trapped protons during solar minimum period, *J. Geophys. Res., 74,* 3575, 1969

Konradi, A., Badhwar, G.D., and Braby, L.A., Recent space shuttle observations of the south atlantic anomaly and the radiation belt models, *Adv. Space Res., 14,* 911, 1994

Kruglanski, M. Heynderickx, D., and Lemaire, J., Proton Anisotropy, *TREND-3 final report, Radiation environments of astronomy missions and LEO missions,* 35 pp., BIRA-IASB, Belgium,1998

Lenchek, A.M. and Singer, S.F., Effects of the finite gyroradii of geomagnetically trapped protons, *J. Geophys. Res., 67,* 4073, 1962

Ljungfelt, S., Calibration of the Radiation Environment Monitor, *Ann. Report, IIIA,*, 153 pp., Paul Scherrer Institute, 5232 Villigen PSI, Switzerland, 1993

Looper, M.D., Blake, J.B., Mewaldt, R.A., Maps of hydrogen isotopes at low altitudes in the inner zone from SAMPEX observations, *Adv. Space Res.., 21,* 1679, 1998

P. Bühler, A. Zehnder., Laboratory for Astrophysics, Paul Scherrer Institute, 5232 Villigen, PSI, Switzerland (e-mail: paul.buehler@psi.ch; alex.zehnder@psi.ch)

M. Kruglanski, Belgian Institute for Space Aeronomy, 1180 Brussels, Belgium (e-mail: michelk@mail.magnet.oma.be)

E. Daly, ESTEC, NL-2200 AG Noordwijk, The Netherlands (e-mail: eamonn@wm.estec.esa.nl)

Received January 3, 1996; revised February 27, 1996; accepted March 31, 1996.

This preprint was prepared with AGU's LaTeX macros v5.01. File ew˙paper formatted February 25, 2000.

Figure 1. REM count rates, representing $> 200\ MeV$ protons, versus B at $1.3 < L < 1.35\ R_E$ for west (asterisks) and east (diamonds) looking detector. The small panels show detector histograms at the lowest B-value for west (upper panel) and east (lower panel) oriented detector. The bias to higher detector channels in the east-histogram indicates a soft incident proton spectrum.

Figure 2. Grey-scale maps of the (left panel) $100\ MeV$ proton flux west-east ratio and (right panel) spectral powerlaw west-east ratio. The ratios are decreasing functions of L and become 1 above $L \approx 1.7\ R_E$.

Figure 3. Local model parameters as function of L. The two uppermost panels show the proton spectral normalisation at $30\ MeV$ and the power law spectral indices for west (asterisks) and east (diamonds) looking detector. The following panels show the west-east ratio, cosine of local magnetic field line dip angle, atmospheric scale height H_0, and altitude power law index n at different energies. The curves show the values of the B-L-bins with the lowest B-value encountered by Mir at a given L.

Figure 4. Generalized model parameters as function of L. The panels show (t.t.b.) the perpendicular proton flux $f_\perp$, its derivative, and the model parameter $\left.\frac{\partial f_p}{\partial L}\right|_{B,E}$.

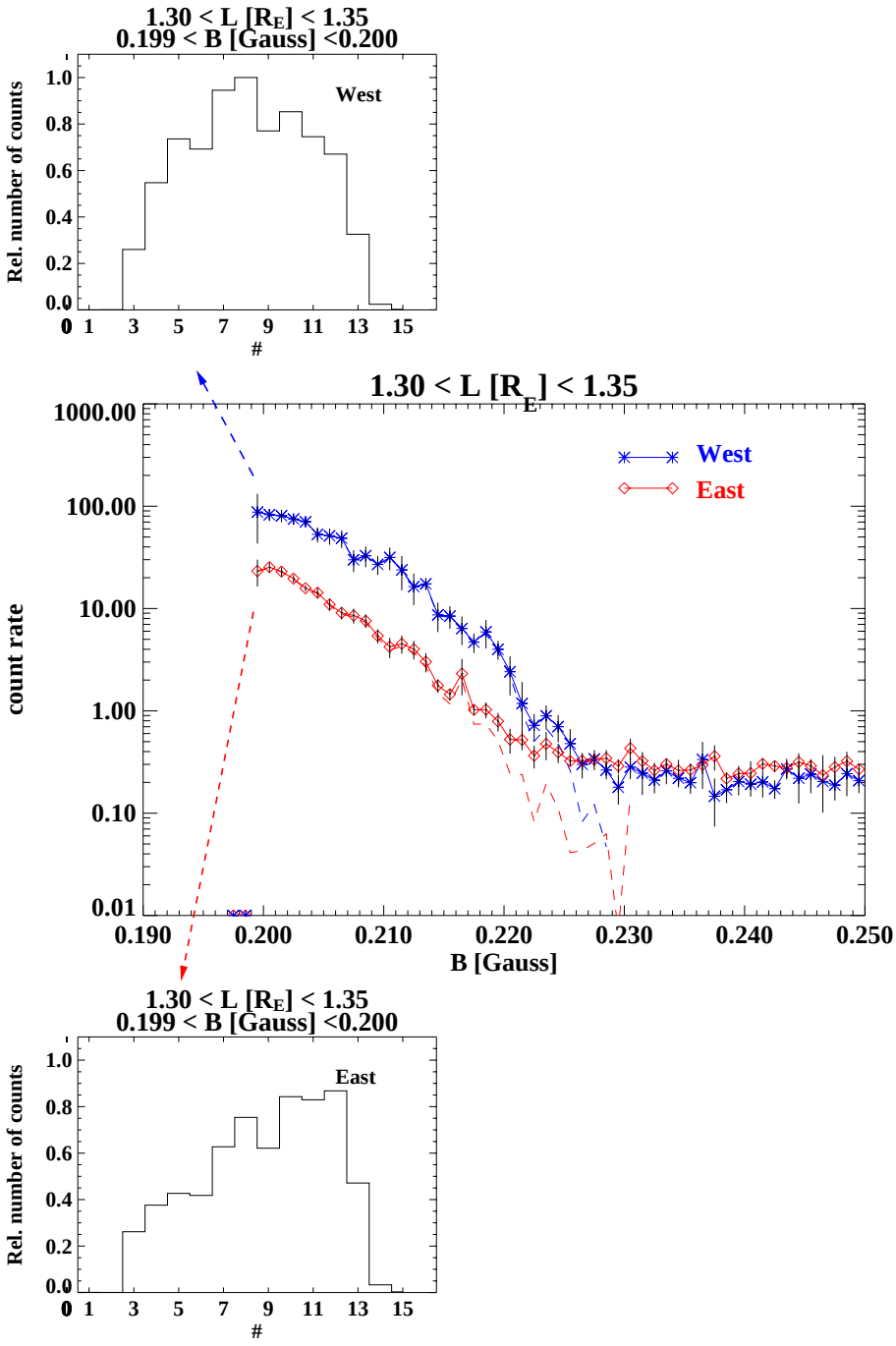
1.30 < L [R_E] < 1.35
0.199 < B [Gauss] <0.200
West
Rel. number of counts
#
1.30 < L [R_E] < 1.35
West
East
count rate
B [Gauss]
1.30 < L [R_E] < 1.35
0.199 < B [Gauss] <0.200
East
Rel. number of counts
#

Figure 1.

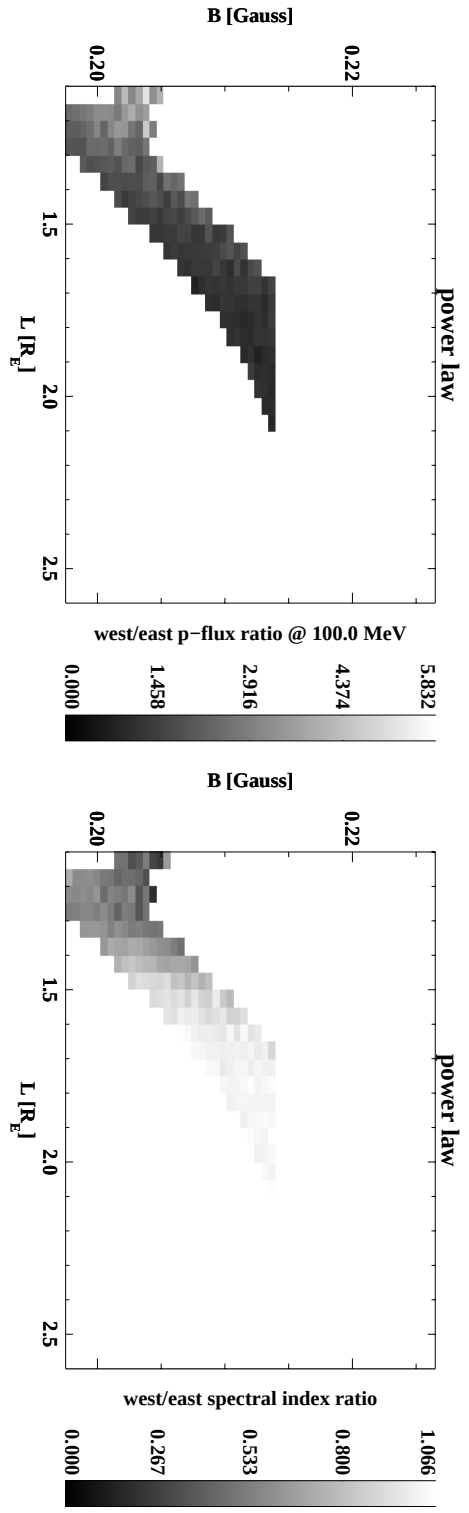
B [Gauss]
0.20
0.22
1.5
2.0
2.5
L [R_E]
power law
west/east p−flux ratio @ 100.0 MeV
0.000
1.458
2.916
4.374
5.832
B [Gauss]
0.20
0.22
1.5
2.0
2.5
L [R_E]
power law
west/east spectral index ratio
0.000
0.267
0.533
0.800
1.066

Figure 2.

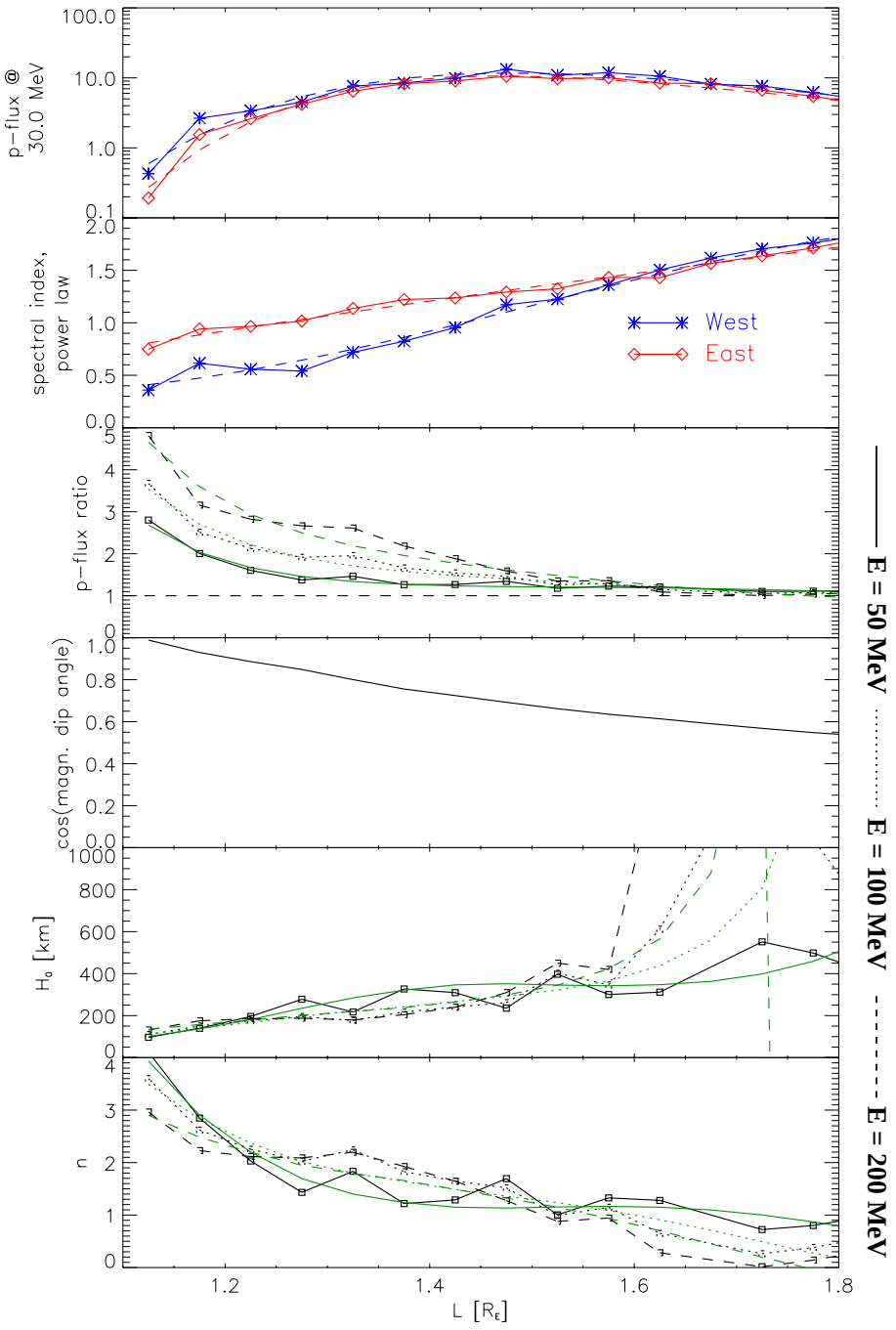
p−flux @ 30.0 MeV
spectral index, power law
West
East
p−flux ratio
cos(magn. dip angle)
H₀ [km]
n
L [R_E]
E = 50 MeV
E = 100 MeV
E = 200 MeV

Figure 3.

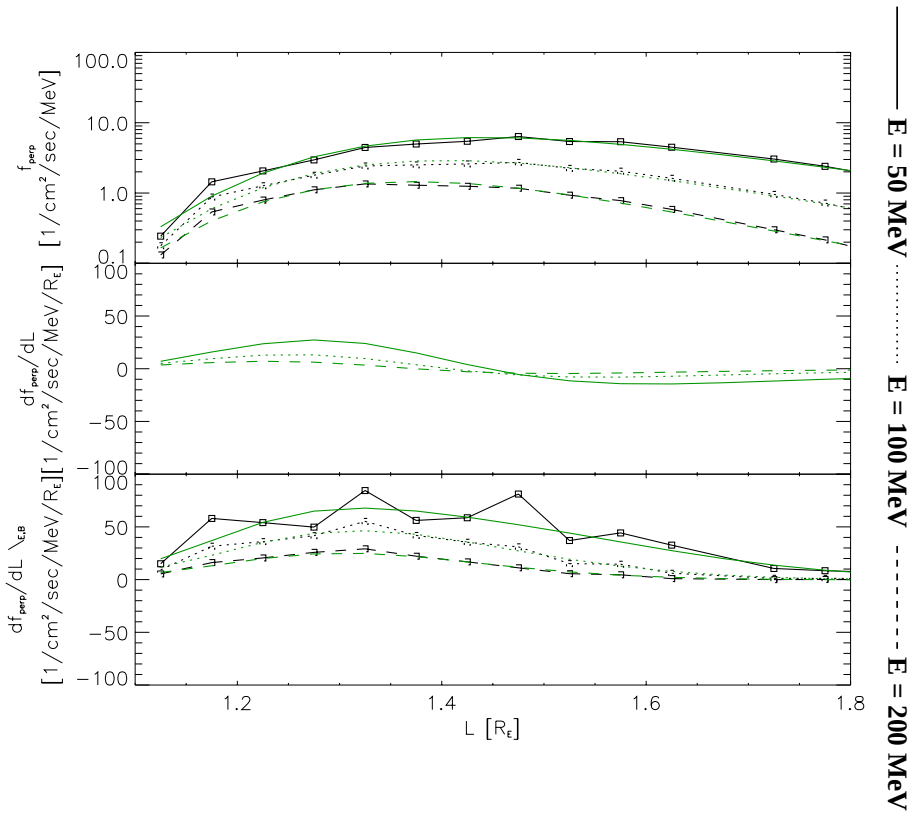
E = 50 MeV
E = 100 MeV
E = 200 MeV
f_perp [1/cm²/sec/MeV]
df_perp/dL [1/cm²/sec/MeV/R_E]
df_perp/dL _E,B [1/cm²/sec/MeV/R_E]
L [R_E]

Figure 4.

Table 1. Atmospheric density - altitude relations and resulting west-east proton flux ratios.

Atmospheric density model $\rho_{atm} \propto$	west-east ratio $f_{west}/f_{east} =$	free parameter
[1] $exp(-h/H_0)$	$exp(dh/H_0)$	$H_0 = dh/ln(f_{west}/f_{east})$
[2] h_0^{-n}	$\left(\frac{h_0+dh/2}{h_0-dh/2}\right)^n$	$n = \frac{ln(f_{west}/f_{east})}{ln\left(\frac{h_0+dh/2}{h_0-dh/2}\right)}$

[1] [*Lenchek and Singer,* 1962]
[2] [*Heckman and Nakano,* 1969]